Chemical Engineering Journal 152 (2009) 583–590

Contents lists available at ScienceDirect

Chemical Engineering Journal

journal homepage: www.elsevier.com/locate/cej

# Catalytic combustion of dilute acetone over Cu-doped ceria catalysts

Chaoquan Hu[a,b], Qingshan Zhu[a,*], Zheng Jiang[a], Lin Chen[a,b], Rongfang Wu[a,b]

[a] State Key Laboratory of Multiphase Complex System, Institute of Process Engineering, Chinese Academy of Sciences, Beijing 100190, China
[b] Graduate School of Chinese Academy of Sciences, Beijing 100049, China

ARTICLE INFO

*Article history:*
Received 23 February 2009
Received in revised form 19 May 2009
Accepted 21 May 2009

*Keywords:*
Catalytic combustion
Acetone
$Cu_xCe_{1-x}O_y$
Lattice oxygen

ABSTRACT

$Cu_xCe_{1-x}O_y$ ($x = 0.06$, 0.13, and 0.23) were prepared by a solution combustion route using glycine as the fuel and tested for the catalytic combustion of dilute acetone in air. The structural characteristics of the catalysts were investigated by specific surface area, X-ray diffraction (XRD), scanning electron microscopy (SEM), X-ray photoelectron spectroscopy (XPS), and temperature-programmed reduction (TPR) techniques. The results reveal that the state of the CuO depends on the Cu/Ce molar ratio in the catalyst, which strongly influences the redox behavior and the catalytic activity of the sample. Among the three catalysts, $Cu_{0.13}Ce_{0.87}O_y$ was found to be the most active in the catalytic combustion of acetone. The pulse reaction of pure acetone in the absence of $O_2$ over the $Cu_{0.13}Ce_{0.87}O_y$ catalyst indicated the participation of lattice oxygen from the catalyst in the acetone combustion. Furthermore, the effect of the acetone concentration and the gas hourly space velocity (GHSV) on the catalytic behavior of the catalyst was examined. The stability of the $Cu_{0.13}Ce_{0.87}O_y$ catalyst for acetone combustion was also investigated and an obvious deactivation was observed under the reactant stream for 35 h at 260 °C. XRD analysis of the deactivated catalyst showed that the formation of bulk CuO was responsible for the deactivation of the catalyst.



## 1. Introduction

In recent years, there are increasing concerns over the abatement of volatile organic compounds (VOCs) since their emission is hazardous to environment and human health [1]. Many different technologies have been developed for the abatement of industrial VOCs emissions in the last few decades, such as physical adsorption, thermal incineration, and catalytic oxidation. Though the physical adsorption with porous materials is effective for eliminating VOCs emission in a certain short period, the overall efficiency of these adsorbent materials is not promising due to their limited removal capacities [2]. Incineration is another convenient way to convert VOCs into nontoxic carbon dioxide and water. However, the conventional thermal incineration requires a high operating temperature (usually exceeds 750 °C) to remove VOCs and consumes significant amounts of energy. Catalytic oxidation has been recognized as one of the most promising techniques for the abatement of VOCs [3,4]. Compared with the above two techniques, catalytic oxidation can remove the dilute VOCs from effluents to very low levels, which may satisfy the stringent environmental regulations. Furthermore, catalytic oxidation is always operated at a relatively low temperature (<500 °C), resulting in a more economical process and reducing the potential for the production of toxic by-products such as $NO_x$. The performance of catalytic combustion strongly depends on the catalyst used in this technique.

Among all the VOCs, acetone is a common organic solvent extensively used in the manufacture of plastics, fibers, drugs, and other chemicals. It can cause environmental hazards and be harmful to the human health. For example, inhalation of acetone vapor can irritate the respiratory tract and cause coughing, dizziness, dullness, and headache. Higher concentrations can produce central nervous system depression, narcosis, and unconsciousness. It is necessary to remove acetone in the gas stream before its emission to the atmosphere. For the catalytic combustion of acetone, both supported noble metal catalysts and metal oxides have been investigated [5–10]. Among the two types of catalysts, the use of the transition metal oxides would be more favorable for industrial applications due to their significantly lower cost than the noble metals.

The unique features of oxygen storage capacity have made $CeO_2$ essential in numerous catalytic oxidation processes [11,12]. Better redox properties than that of pure $CeO_2$ are obtained by the incorporation of metal ions into the $CeO_2$ lattice forming $Ce_{1-x}M_xO_y$ solid solutions, such as Ni, Zr, and Mn [13–17]. Recent reports have shown that the performance of Ce-based oxides in oxidation reactions is greatly enhanced by incorporation of CuO into $CeO_2$ lattice, and the activity of $CeO_2$ supported CuO catalyst for oxidation reaction is even comparable to that of the supported noble metal catalysts [18]. Therefore, Cu-doped ceria is expected to be a good candidate for catalytic combustion of acetone. Although the CuO–$CeO_2$ catalyst has

* Corresponding author. Tel.: +86 10 62536108; fax: +86 10 62536108.
*E-mail address:* qszhu@home.ipe.ac.cn (Q. Zhu).

1385-8947/$ – see front matter © 2009 Elsevier B.V. All rights reserved.
doi:10.1016/j.cej.2009.05.033

been widely investigated for the oxidation of CO and hydrocarbons [19–21], to our best knowledge the catalytic combustion of acetone over Cu-doped $CeO_2$ has not been reported.

In order to truly assess the effect of the $Cu_xCe_{1-x}O_y$ composition, a single synthesis and homogeneous mixed oxides are needed [22]. It has been reported that solution combustion synthesis can produce homogeneous high-purity powder in a short time at a low cost with a simple equipment [23]. This method involves the ignition of precursor salt solution containing the required metal ions and an organic fuel. During the combustion process, a large amount of gaseous products are produced, which can achieve the mutual dispersion of oxides and homogeneous powders.

The aim of the present work is to prepare $Cu_xCe_{1-x}O_y$ catalysts via a nitrate–glycine solution combustion route and evaluate their catalytic performance for acetone combustion in air. The structure properties of the catalysts were characterized by XRD, SEM, XPS, and $H_2$-TPR measurements. The mechanism of the acetone combustion over $Cu_{0.13}Ce_{0.87}O_y$ was studied by carrying out pulse reaction of pure acetone in the absence of $O_2$ over the catalyst. Furthermore, the stability of the $Cu_{0.13}Ce_{0.87}O_y$ catalyst for the acetone combustion, as well as the reason for the catalyst deactivation, was investigated.

## 2. Experimental

### 2.1. Catalyst preparation

All chemical reagents in this experiment were of analytical grade and used as received without further purification. The $Cu_xCe_{1-x}O_y$ catalysts were prepared by a combustion method using $Ce(NO_3)_3{\cdot}6H_2O$, $Cu(NO_3)_2{\cdot}3H_2O$ and glycine as raw materials. Specifically, $Ce(NO_3)_3{\cdot}6H_2O$, $Cu(NO_3)_2{\cdot}3H_2O$, and glycine were dissolved in deionized water to form a solution with the metal ion concentration of 0.2 M. The molar ratio of glycine/nitrate in the solution was 0.80. The precursor solution was then heated in an evaporating dish under continuous stirring, until the solution got ignited spontaneously and resulted in porous, foamy and fragile materials. The resulting powders were further calcined at 500 °C for 6 h. The actual CuO content in the catalyst was analyzed by ICP-AES. The notation of *x*, *y* in the samples means the atomic ratio.

### 2.2. Catalyst characterizations

The composition of the $Cu_xCe_{1-x}O_y$ was determined by inductively coupled plasma atomic emission spectroscopy (ICP-AES) on a PE OPTIMA 5300DV spectrometer. The phase structure of all the samples was analyzed by an X-ray diffractometer (X'Pert MPD Pro, PANalytical, The Netherlands). The morphology was examined by field-emission scanning electron microscopy (FESEM, JSM-6700F, JEOL). The BET surface area of each sample was determined using the Autosorb-1 (Quantachrome Instruments) gas adsorption system. Prior to each analysis, the samples were dried at 300 °C for 4 h under vacuum. The BET surface area was calculated using a five-point isotherm. X-ray photoelectron spectroscopy (XPS) data were obtained with an ESCALab220i-XL electron spectrometer from VG Scientific using 300W Al Kα radiation. The binding energy was referenced to the C1s line at 284.8 eV from adventitious carbon.

Temperature-programmed reduction (TPR) experiments were carried out using a CHEMBET 3000 adsorption instrument (Quantachrome, USA) equipped with a thermal conductivity detector (TCD). About 20 mg samples were loaded and pretreated with Ar at 150 °C for 30 min. After the sample was cooled down to 50 °C, a reduction agent of 5% $H_2$/Ar with a flow rate of 20 mL/min was introduced, and the sample was heated up to 700 °C with a heating rate of 10 °C/min. Calibration of the amount of $H_2$ consumed was carried out on the basis of the amount of $H_2$ needed for the reduction of pure CuO.

The pulse experiment was performed in a microreactor with diameter of 4 mm and length of 30 cm. 0.1 g of catalyst (20–40 mesh) was loaded into the microreactor in a constant temperature zone and packed between two quartz wool plugs. Before carrying out the pulse reaction, the catalyst was treated in situ at 150 °C in the flow of He for 1 h. A pulse of acetone of 100 μL (vaporized at 100 °C) was injected into a He carrier stream (30 mL/min) using a microsyringe at the interval of 20 min. The temperature of the He carrier was controlled by a heating belt and remained in the range of 100–105 °C before entering the microreactor. The concentration of acetone was determined by the gas chromatograph (GC) with a flame ionization detector (TP-2060F, FID).

### 2.3. Catalytic performance evaluation

The catalytic activity of the catalyst was assessed by conducting the complete oxidation test for acetone in a tubular reactor with a diameter about 8 mm. The catalyst powder with a size of 20–40 mesh was used for the catalytic evaluation. In each test run, 0.2 g of catalyst diluted with silica (20–40 mesh) was placed at the center of the reactor. The temperature was monitored by a thermocouple located above the catalyst. The acetone vapor was carried by an air stream bubbling through a boat-shaped saturator in ice-bath. The air contained concentrated acetone vapor was further diluted with another airflow before reaching the catalyst bed. The concentration of acetone was controlled by adjusting the air stream flowing through the saturator and always confirmed by the GC. The total flow rate was set at 200 mL/min. To prevent the physisorption of acetone in the initial stages of the test, the catalyst was pretreated at 100 °C for 30 min under the test flows of reactant mixture (1000 ppm acetone balanced by dry air). When a steady state was attained, the temperature was raised stepwise per 10 °C from 100 °C to the temperature that could achieve the complete conversion of acetone. The acetone concentration in the stream was determined by the GC (TP-2060F, FID), while the $CO_2$ was analyzed by a GC with a TCD (SP-3420). The detection limit is 1 ppm for acetone and 5 ppm for carbon dioxide. In all reaction conditions, the carbon mass balances are in the range 100 ± 5%. The reaction rate for acetone combustion ($-R_{acetone}$) was calculated according to

$$-R_{acetone} = \frac{X_{acetone}}{W/F_{acetone,0}}$$

where $X_{acetone}$ is the measured acetone conversion and $W/F_{acetone,0}$ is the space time referring to the amount of catalyst loaded into the reactor and the inlet acetone molar flow rate. The $X_{acetone}$ value was chosen to be lower than 5%.

Long-term stability test over the catalyst was carried out under conditions similar to the activity evaluation. The catalyst bed was first heated to 300 °C at which a complete acetone conversion was achieved, then decreased to 260 °C, and maintained constant at this temperature for about 35 h.

## 3. Results and discussion

Fig. 1 shows the XRD patterns of the as-prepared $Cu_xCe_{1-x}O_y$ samples with different CuO contents. The distinct fluorite oxide diffraction pattern of $CeO_2$ can be seen in the three samples. No CuO phase can be identified for the $Cu_{0.06}Ce_{0.94}O_y$ and the $Cu_{0.13}Ce_{0.87}O_y$ samples, whereas apparent CuO diffraction peaks appear for the $Cu_{0.23}Ce_{0.77}O_y$ sample. This result is good agreement with the previous report concerning the structure features of $Cu_xCe_{1-x}O_y$ calcined at 500 °C, where the CuO diffraction peaks began to appear when the Cu/(Cu + Ce) ratio ≥0.15 [24]. For $Cu_{0.06}Ce_{0.94}O_y$ and $Cu_{0.13}Ce_{0.87}O_y$, the absence of CuO diffraction peaks is commonly

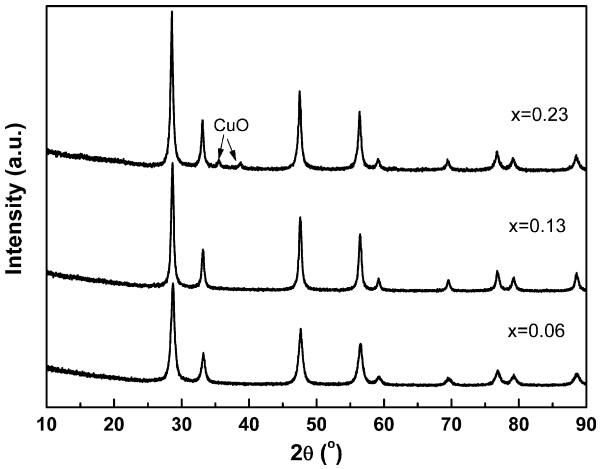


**Fig. 1.** XRD patterns of the as-prepared $Cu_xCe_{1-x}O_y$ samples.

explained that either the CuO is amorphous or incorporated into the $CeO_2$ lattice, or it is well dispersed on the surface of $CeO_2$ in the form of small clusters that cannot be detected by XRD [25]. Taking the calcination temperature into account, the calcination temperature in the present study is high enough for the formation of CuO crystalloid. Thus, it is highly possible that the CuO was well dispersed on the surface of $CeO_2$, or incorporated into the $CeO_2$ lattice, or a combination of these two states.

It should be noted that the position of $CeO_2$ diffraction peaks slightly shifted to low $2\theta$ values with increasing the Cu level from 0.06 to 0.23, suggesting more amounts of CuO were incorporated into the $CeO_2$ lattice since the radius of $Cu^{2+}$ (0.072 nm) is smaller than that of the $Ce^{4+}$ ions (0.092 nm). This is further confirmed by comparison of the lattice parameter calculated from the (3 1 1) crystallographic plane [26]. As shown in Table 1, the lattice constant slightly decreased with the increase of the CuO content in the sample. In addition, all the calculated lattice constants were lower than that of pure $CeO_2$ (0.5423 nm, not shown), confirming that certain amounts of CuO was incorporated into the $CeO_2$ lattice. The crystallite size of the $CeO_2$ is also influenced by the Cu doping. The average crystallite sizes of the samples were obtained according to the Scherrer equation by measuring the (1 1 1) diffraction of the cubic crystallites and shown in Table 1. The size increased from 13 nm for $Cu_{0.06}Ce_{0.94}O_y$ to 26 nm for $Cu_{0.23}Ce_{0.77}O_y$. This may be caused by the different degree of sintering for ceria due to the Cu ions incorporating into the defect sites.

The morphologies of the as-prepared samples were examined by SEM. As shown in Fig. 2, the images revealed that the $Cu_xCe_{1-x}O_y$ samples were highly porous in nature and consisted of foam-like clusters, originating from the rapid production of gaseous products during the combustion process. The BET surface areas of these samples are listed in Table 1. It can be seen that the BET surface area decreased from 32.8 to 11.4 $m^2/g$ with the increase of the Cu/(Cu + Ce) molar ratio from 0.06 to 0.23, indicating the Cu/Ce has effect on the textural properties of the $Cu_xCe_{1-x}O_y$ samples. Two modes, namely grain boundary formation and crystallite growth, are often accounted for the decrease of surface area [27]. It appears

**Table 1**
Crystallite size, lattice constant, and specific surface area of the $Cu_xCe_{1-x}O_y$ samples.

| Sample | Crystallite size (nm) | Lattice constant (nm) | Surface area ($m^2/g$) |
|---|---|---|---|
| $Cu_{0.06}Ce_{0.94}O_y$ | 13 | 0.5418 | 32.8 |
| $Cu_{0.13}Ce_{0.87}O_y$ | 15 | 0.5415 | 27.1 |
| $Cu_{0.23}Ce_{0.77}O_y$ | 26 | 0.5413 | 11.4 |

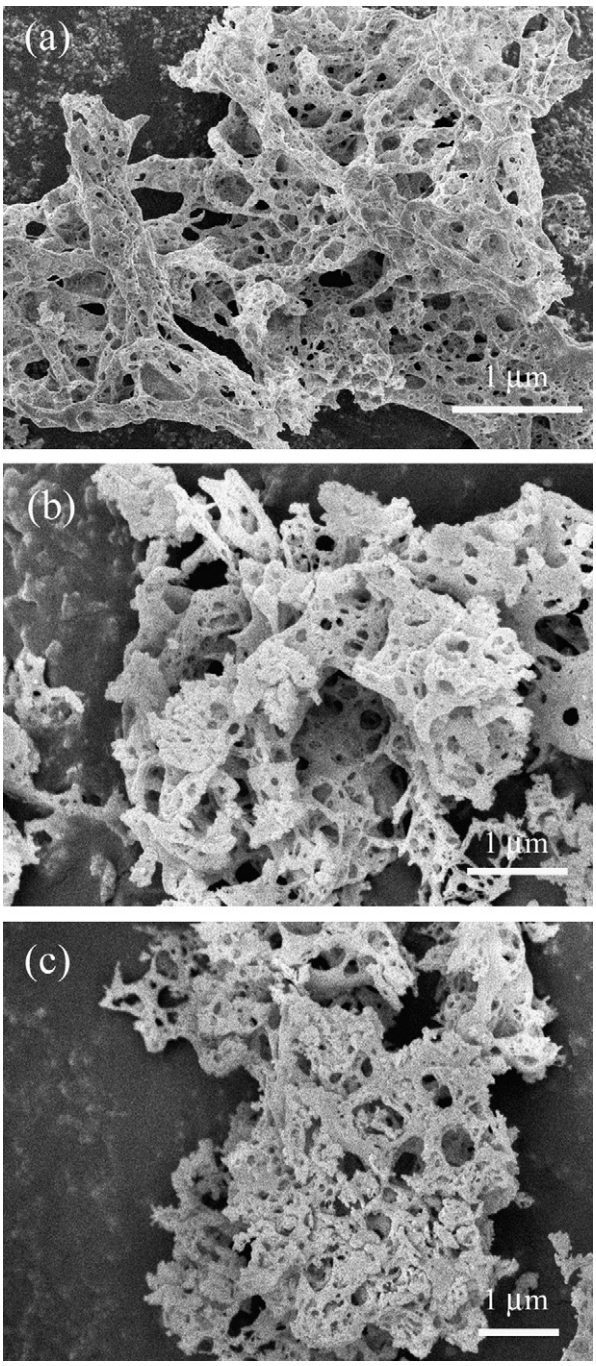


**Fig. 2.** SEM images of the $Cu_xCe_{1-x}O_y$ samples: (a) $Cu_{0.06}Ce_{0.94}O_y$, (b) $Cu_{0.13}Ce_{0.87}O_y$, and (c) $Cu_{0.23}Ce_{0.77}O_y$.

that the steady decline in the surface areas can be attributed to the growth of the crystallite size, as discussed in the XRD measurement.

The surface compositions of all the $Cu_xCe_{1-x}O_y$ samples were further studied by XPS. Fig. 3a shows the Cu 2p XPS of all the samples. It can be seen that the spectra of Cu $2p_{3/2}$ in all the samples contained an obvious shake-up peak at 939–944 eV and a main peak at 933.6 eV. It has been accepted that the presence of the shake-up peak and a higher Cu $2p_{3/2}$ binding energy (933.0–933.8 eV) are two major XPS characteristics of $Cu^{2+}$, while a lower Cu $2p_{3/2}$ binding energy (932.2–933.0 eV) and the absence of the shake-up peak are characteristics of reduced copper [28]. Thus, the valence of Cu atom in these samples should be +2. For the Ce 3d spectra of the three samples (Fig. 3b), the six peaks associated with the four-valent Ce

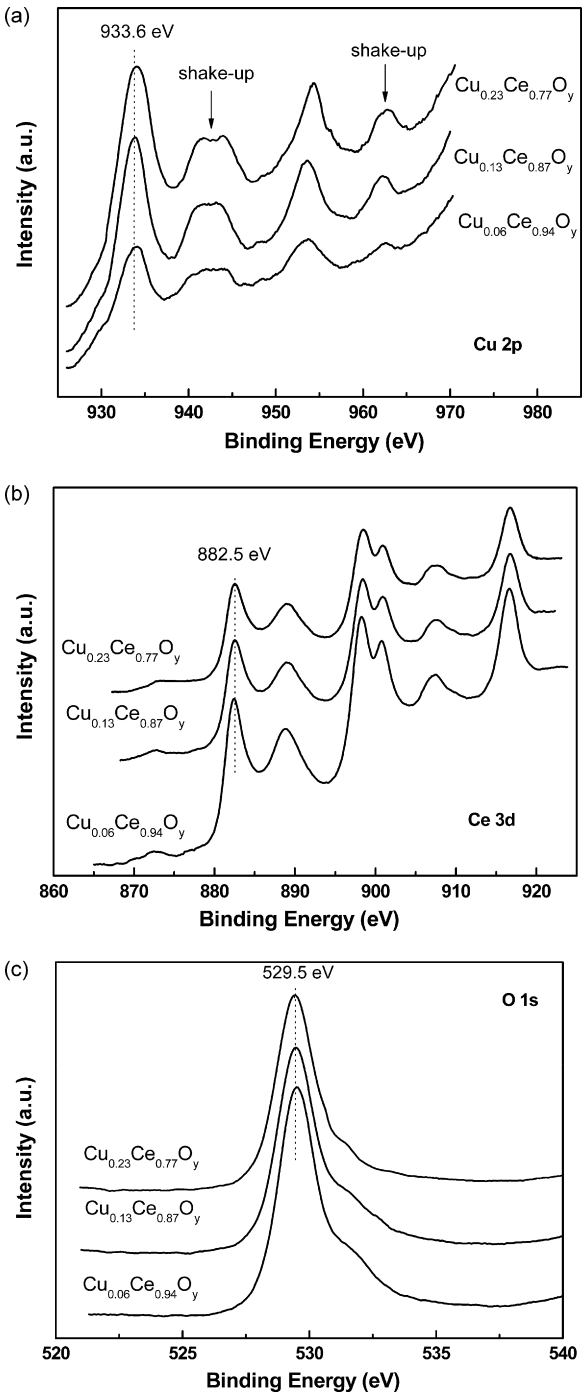


**Fig. 3.** XPS of the $Cu_xCe_{1-x}O_y$ samples: (a) Cu 2p, (b) Ce 3d, and (c) O 1s.

$4f^0$ can be seen [28]. The bands at 903.2–903.5 eV and 884–886 eV represented the $3d^{10}4f^1$ initial electronic state corresponding to $Ce^{3+}$ ions was not observed, indicating the valence of Ce atom was +4. In the case of O 1s (Fig. 3c), a main peak centered at 529.5 eV and a small shoulder can be seen. The peak at the binding energy of about 529.5 eV can be seen as lattice oxygen of the oxides in the sample, while the shoulder can be ascribed to the oxygen adsorbed on the surface [28]. The XPS results indicate that the valence of the each element in the three samples was identical.

The surface composition, expressed as Cu/(Cu + Ce) molar ratio, is shown in Table 2. In all cases, the surface Cu/(Cu + Ce) ratio is higher than the nominal value, indicating not all the $Cu^{2+}$ was incorporated into the $CeO_2$ lattice. For the $Cu_{0.06}Ce_{0.94}O_y$ and the

**Table 2**
XPS result and $H_2$ uptake of the $Cu_xCe_{1-x}O_y$ samples.

| Sample | Cu/(Cu + Ce) (mol%) | | $H_2$ uptake (mmol/$g_{cata}$) | |
|---|---|---|---|---|
| | Nominal | XPS | Nominal | Actual |
| $Cu_{0.06}Ce_{0.94}O_y$ | 6 | 9 | 0.24 | 0.46 |
| $Cu_{0.13}Ce_{0.87}O_y$ | 13 | 20 | 0.81 | 1.22 |
| $Cu_{0.23}Ce_{0.77}O_y$ | 23 | 38 | 1.53 | 1.73 |

$Cu_{0.13}Ce_{0.87}O_y$ samples, no diffraction peaks of CuO in the XRD pattern were observed. Thus, it may be concluded that the highly dispersed CuO and $Cu^{2+}$ in the $CeO_2$ coexist in the two samples, which is further confirmed by the TPR measurement in the following paragraph. As for the $Cu_{0.23}Ce_{0.77}O_y$, CuO phase was detected by the XRD. So it is highly possible that three different CuO species, highly dispersed CuO, $Cu^{2+}$ in the $CeO_2$ lattice, and bulk CuO, may coexist in this sample.

The state of the CuO in the $Cu_xCe_{1-x}O_y$ samples was further investigated by $H_2$-TPR measurement. The TPR profiles of $Cu_xCe_{1-x}O_y$ samples are shown in Fig. 4. Obviously, the reduction behaviors of the $Cu_xCe_{1-x}O_y$ samples depend on the composition. The profiles of the $Cu_{0.06}Ce_{0.94}O_y$ and the $Cu_{0.13}Ce_{0.87}O_y$ samples show two reduction peaks (α and β) in the range of 150–300 °C and the area of β is always larger than that of peak α, indicating there were two types of CuO in the samples. Although the presence of two reduction peaks for CuO–$CeO_2$ with a low CuO content is a common feature of CuO–$CeO_2$ catalyst [29–33], the interpretation for the peaks is different. Liu and Flytzani-Stephanopoulos ascribed the low reduction temperature peak to the CuO clusters strongly interacting with $CeO_2$ and the high reduction temperature peak to the larger CuO particles non-associated with $CeO_2$ [30]. Luo et al. believed that the low reduction temperature peak was due to the reduction of highly dispersed CuO species on the surface of the catalyst and the other peak corresponded to the reduction of $Cu^{2+}$ penetrated into the $CeO_2$ lattice [31].

In the present study, the XRD results did not show any diffraction peaks of CuO in the $Cu_xCe_{1-x}O_y$ mixed oxides at a low CuO content and the XPS results indicated the enrichment of CuO on the surface of the two samples. Thus, it is more likely that the peak α is due to the reduction of finely dispersed CuO on the surface, the peak β is due to the reduction of $Cu^{2+}$ ions in $Cu_xCe_{1-x}O_y$ solid solution. For the sample $Cu_{0.23}Ce_{0.77}O_y$, in which bulk CuO becomes present, a new peak γ is found in the $H_2$-TPR profile, suggesting that the peak γ is due to the reduction of bulk CuO. It should be noted that the α peak in the TPR profile for the $Cu_{0.23}Ce_{0.77}O_y$ sample almost disappears, indicating that a poor dispersion of CuO on the surface of the catalyst.

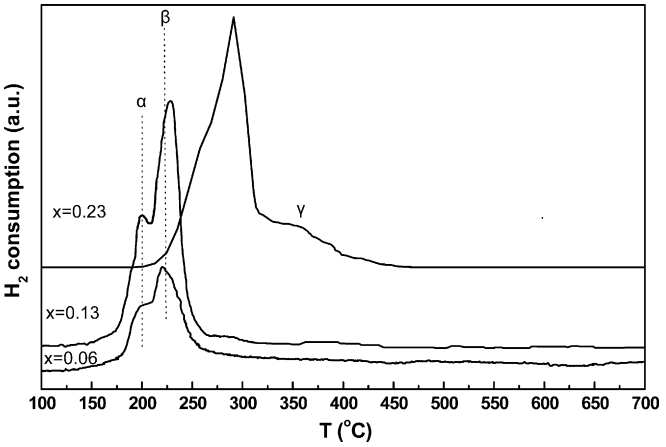


**Fig. 4.** $H_2$-TPR profiles of the $Cu_xCe_{1-x}O_y$ samples.

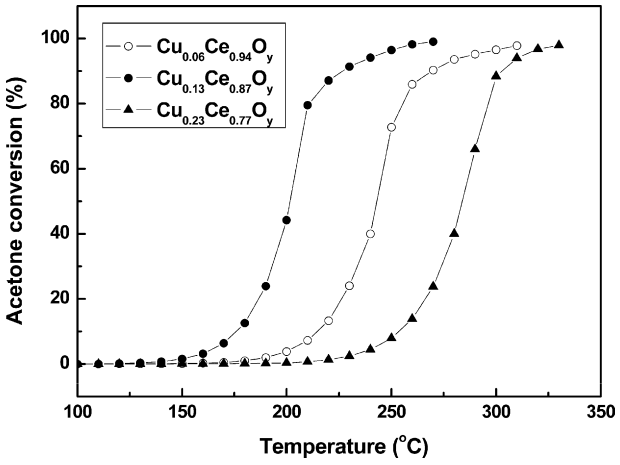


**Fig. 5.** Light-off curves for acetone combustion over the as-prepared $Cu_xCe_{1-x}O_y$ samples. Acetone concentration = 1000 ppm and GHSV = 15 000 $h^{-1}$.

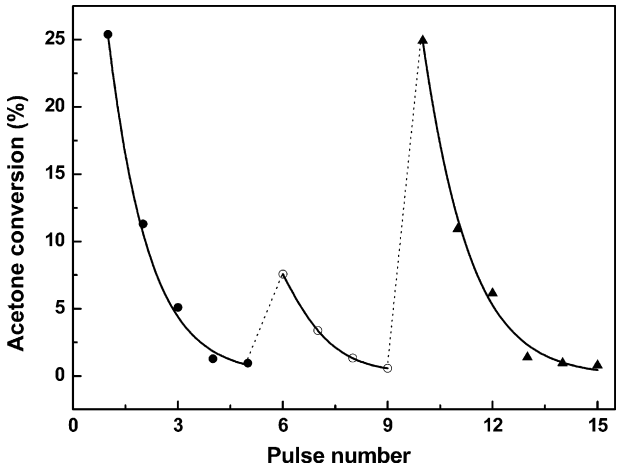


**Fig. 6.** Acetone conversion with pulse number in the pulse reaction of acetone over the $Cu_{0.13}Ce_{0.87}O_y$ catalyst in the absence of oxygen at 250 °C: (●) fresh catalyst; (○) after aged under He at 500 °C for 1 h; (▲) after reoxidized by $O_2$ at 500 °C for 1 h.

The reduction temperatures of the two peaks for the $Cu_{0.06}Ce_{0.94}O_y$ and the $Cu_{0.13}Ce_{0.87}O_y$ samples are almost the same, while those of the $Cu_{0.23}Ce_{0.77}O_y$ sample are much higher. The difference of the crystallite size and the BET surface area among the three samples may be responsible for their redox behaviors. The $Cu_{0.23}Ce_{0.77}O_y$ sample has the largest crystallite size and the lowest BET surface area, which may lower the reducibility of the sample and lead to the increase of the reduction temperature. In addition, the finely dispersed CuO species that are easily reduced to metallic Cu and the effect of hydrogen spillover on the metallic Cu can also result in the decrease of the reduction temperature of CuO incorporated into the $CeO_2$ lattice [32]. The quantitative analysis of the reduction peaks was further carried out and the results are shown in Table 2. The data for the hydrogen uptake during the TPR show that the amount of the consumed $H_2$ is higher than the value required for the complete reduction of CuO to Cu, indicating the reduction of $CeO_2$ also took place alongside with the CuO reduction. This phenomenon may be related to the presence of metallic Cu that may act as a catalyst for $H_2$ dissociation [34], which can provide atomic hydrogen and thus facilitate the reduction of $CeO_2$ at low temperature.

Fig. 5 shows the light-off curves for acetone combustion over the as-prepared $Cu_xCe_{1-x}O_y$ catalysts. It should be noted that no by-product for the acetone oxidation was detected for the three catalysts. The light-off curve is often characterized by two parameters, $T_{50\%}$ and $T_{90\%}$. $T_{50\%}$ is the temperature required to achieve 50% conversion and often used as an indicative of the relative activity of the catalysts, while $T_{90\%}$ corresponds to the temperature for 90% conversion. Table 3 lists the values of these parameters for the combustion of 1000 ppm of acetone over the $Cu_xCe_{1-x}O_y$ catalysts. It is clearly observed that the activity of the $Cu_xCe_{1-x}O_y$ strongly depends on the Cu/Ce in the catalyst. Taking the $T_{50\%}$ and $T_{90\%}$ into account, the $Cu_{0.13}Ce_{0.87}O_y$ catalyst appeared to be the most active catalyst with a steep conversion curve, on which the combustion of acetone became appreciable at 180 °C, approaching 50% conversion at 200 °C and quickly reaching above 95% conversion at 232 °C. The catalytic performance of the $Cu_{0.13}Ce_{0.87}O_y$ catalyst is comparable to that of $Pt/Al_2O_3$, which could achieve the 95% conversion of acetone 300 °C [35]. In the case of the $Cu_{0.23}Ce_{0.77}O_y$ catalyst, the obvious reaction started at 250 °C and a higher temperature was required to achieve the 95% conversion of acetone. It appears that the reactivity, the surface area, and the CuO content in the $Cu_xCe_{1-x}O_y$ samples cannot be briefly correlated.

**Table 3**
$T_{50\%}$, $T_{90\%}$, and apparent activation energy (AAE) of acetone combustion over the $Cu_xCe_{1-x}O_y$ samples.

| Sample | $T_{50\%}$ (°C) | $T_{90\%}$ (°C) | AAE (kJ/mol) |
|---|---|---|---|
| $Cu_{0.06}Ce_{0.94}O_y$ | 241 | 266 | 116 |
| $Cu_{0.13}Ce_{0.87}O_y$ | 200 | 223 | 112 |
| $Cu_{0.23}Ce_{0.77}O_y$ | 283 | 305 | 130 |

Two possible mechanisms have been widely accepted now for oxidation reactions: a suprafacial mechanism, which arises from the interaction between surface oxygen and substrate, and an intrafacial mechanism, which involves bulk oxygen migration toward surface for the oxidation of the substrate [36]. Various researchers have pointed out that the combustion of acetone over transition metal oxide catalysts occurs by means of a Mars–van Krevelen type mechanism [37,38]. In particular, Finocchio et al. studied acetone combustion over CuO by FTIR and proposed a Mars–van Krevelen type reaction mechanism [37]. Thus, it is highly possible the acetone combustion over the $Cu_xCe_{1-x}O_y$ catalysts proceeds according to the Mars–van Krevelen mechanism, which involves a redox cycle and is related to the mobility of the lattice oxygen. The oxygen mobility in the crystalline framework is associated to catalyst reducibility that can be studied by TPR: the lower the TPR peak temperature, the higher the mobility of lattice oxygen. Thus, a relationship between catalytic activity and reducibility may be established when the catalyst undergoes a redox cycle.

Taken the TPR results into account, it can be concluded that the mobility of the lattice oxygen in the samples is in the following order: $Cu_{0.13}Ce_{0.87}O_y \approx Cu_{0.06}Ce_{0.94}O_y > Cu_{0.23}Ce_{0.77}O_y$. So, it is reasonable that the $Cu_{0.23}Ce_{0.77}O_y$ shows the lowest catalytic activity for the acetone combustion due to its relatively low mobility of the lattice oxygen. For the $Cu_{0.13}Ce_{0.87}O_y$ and the $Cu_{0.06}Ce_{0.94}O_y$ samples, the difference of the catalytic behavior may be related to the surface structure. The results of the XPS and the TPR have shown that the $Cu_{0.13}Ce_{0.87}O_y$ has more highly dispersed CuO on the surface than the $Cu_{0.06}Ce_{0.94}O_y$. Accordingly, it may be concluded that the highly dispersed CuO on the surface is the active site for the acetone combustion. However, further study is still needed to clarify the exact role of highly dispersed CuO during the acetone combustion over the catalyst.

In order to further understand the role of the lattice oxygen, pulse reaction of acetone over the $Cu_{0.13}Ce_{0.87}O_y$ catalyst in the absence of oxygen was performed. As shown in Fig. 6, the acetone conversion over the fresh catalyst decreased sharply with increasing the pulse number, which is expected due to the consumption of the lattice oxygen on the catalyst surface. After the deactivated cata-

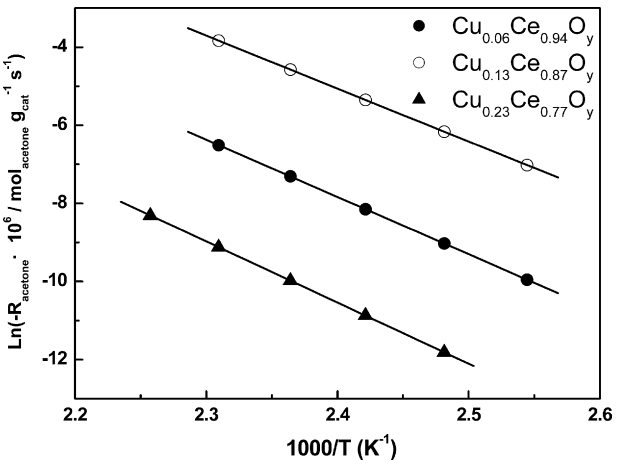


**Fig. 7.** Arrhenius plots of the $Cu_xCe_{1-x}O_y$ catalysts for acetone combustion.

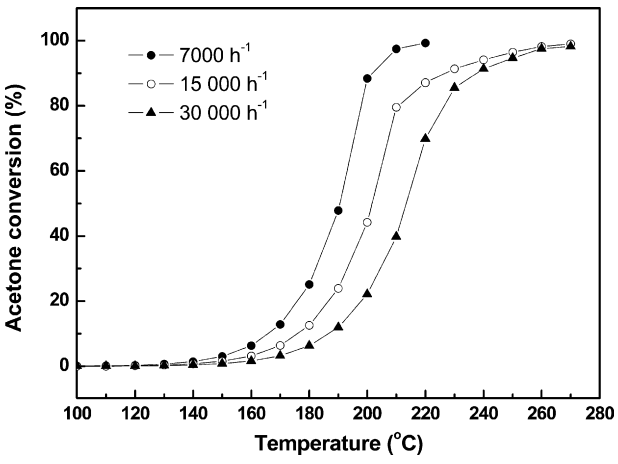


**Fig. 9.** Effect of GHSV on the catalytic performance of the $Cu_{0.13}Ce_{0.87}O_y$ catalyst for the acetone combustion, acetone concentration = 1000 ppm.

lyst was aged under He at 500 °C for 1 h, the acetone conversion was increased slightly, but is still lower than that of the fresh catalyst. This phenomenon may be related to the migration of the subsurface oxygen to the catalyst surface at high temperature. After the 9th pulse, the catalyst was reoxidized by $O_2$ at 500 °C for 1 h and the pulse experiment was continued. The acetone conversion was found to reach its original value at the 10th pulse, suggesting the catalyst regained its original activity. These results indicate that the lattice oxygen from the $Cu_{0.13}Ce_{0.87}O_y$ catalyst plays a very important role in the acetone combustion, which further confirms the Mars–van Krevelen mechanism.

Fig. 7 shows the Arrhenius-type plots for the acetone combustion over the $Cu_xCe_{1-x}O_y$ catalysts. The apparent activation energies (AAE) of the reaction for $Cu_{0.06}Ce_{0.94}O_y$, $Cu_{0.13}Ce_{0.87}O_y$, and $Cu_{0.23}Ce_{0.77}O_y$ are 116, 112, and 130 kJ/mol, respectively. These values are in good agreement with the values reported for acetone combustion over manganese oxide (118–133 kJ/mol) [39]. As discussed in the $H_2$-TPR, the reactivity in the reaction with hydrogen of the lattice oxygen for the catalysts is in the following order: $Cu_{0.13}Ce_{0.87}O_y \approx Cu_{0.06}Ce_{0.94}O_y > Cu_{0.23}Ce_{0.77}O_y$. Thus, the AAE for acetone combustion over the $Cu_{0.13}Ce_{0.87}O_y$ and the $Cu_{0.06}Ce_{0.94}O_y$ samples is very close, while that of the $Cu_{0.23}Ce_{0.77}O_y$ sample is larger.

The effect of the acetone concentration on the catalytic performance of the $Cu_{0.13}Ce_{0.87}O_y$ catalyst for acetone combustion was investigated. As shown in Fig. 8, when the acetone concentration was raised, a higher reaction temperature was required for the complete conversion of acetone. The influence of space velocity on the catalytic performance was also examined over the $Cu_{0.13}Ce_{0.87}O_y$ catalyst. As shown in Fig. 9, increased GHSV led to a lower acetone conversion under a same reaction temperature, which may be caused by the shorter retention time of acetone in the catalyst bed under higher GHSV.

It is known that water is produced during the combustion of VOCs and always has a detrimental effect on the catalyst structure. Hence, the endurance test was also carried out in this work to evaluate the endurance of the $Cu_{0.13}Ce_{0.87}O_y$ catalyst. The acetone concentration was set at 1000 ppm and the reaction temperature was set at 260 °C. The experimental results are shown in Fig. 10. In the initial reaction time, the conversion of acetone slightly decreased from 98.6% to 95.1% and kept constant during the following 12 h. After 35 h on stream, the acetone conversion sharply decreased to 73%, suggesting an obvious deactivation of the catalyst occurred. In order to understand the reason of the deactivation, XRD was used to examine the catalyst tested for 36 h. For comparison, the XRD of the fresh sample is also shown in Fig. 11. It can be seen that the sample tested for 36 h showed obvious CuO diffraction peaks. It is an indication of the formation of bulk CuO, which would inhibit the synergetic effect between the $CeO_2$ and CuO [40].

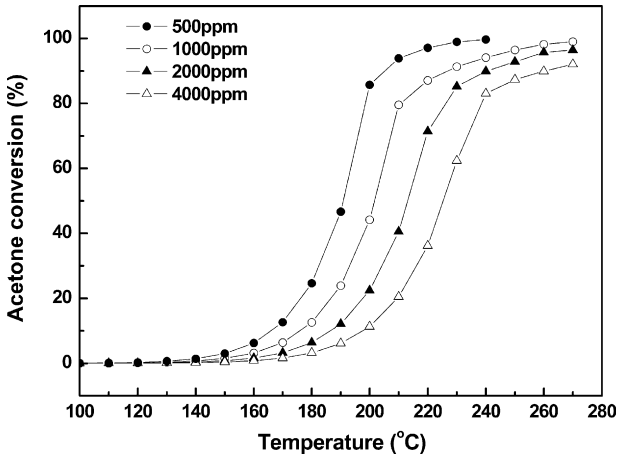


**Fig. 8.** Effect of acetone concentration on the catalytic performance of the $Cu_{0.13}Ce_{0.87}O_y$ catalyst for the acetone combustion, and GHSV = 15 000 $h^{-1}$.

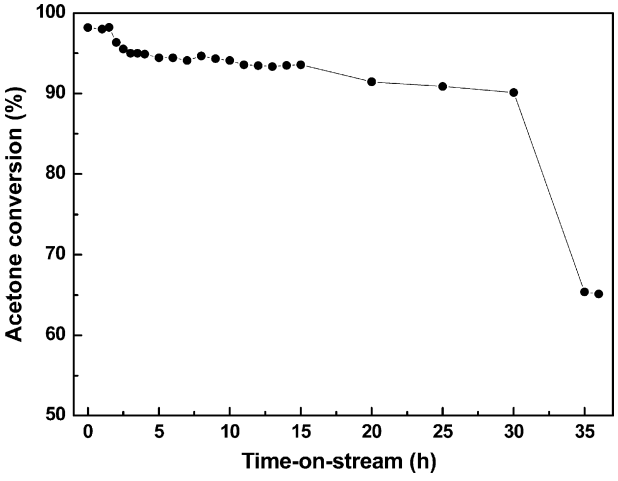


**Fig. 10.** Evolution of acetone conversion at 260 °C with time-on-stream for the $Cu_{0.13}Ce_{0.87}O_y$ catalyst, acetone concentration = 1000 ppm, and GHSV = 15 000 $h^{-1}$.

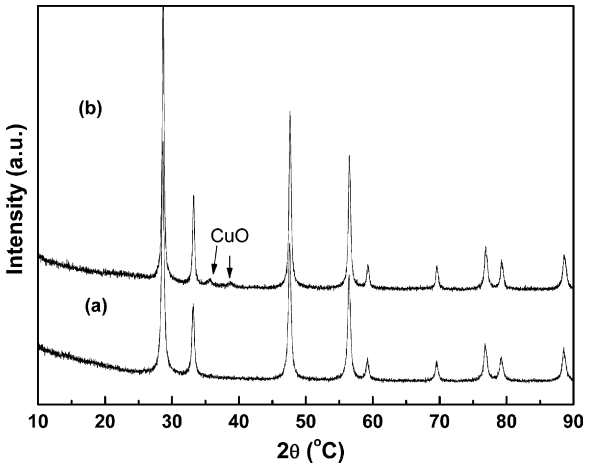


**Fig. 11.** XRD patterns of the $Cu_{0.13}Ce_{0.87}O_y$ catalyst: (a) before test and (b) after tested for 36 h.

Thus, it can be concluded that the loss of the acetone conversion over the $Cu_{0.13}Ce_{0.87}O_y$ catalyst mainly results from the decrease of the CuO dispersion on the catalyst surface.

## 4. Conclusions

$Cu_xCe_{1-x}O_y$ ($x = 0.06$, 0.13, and 0.23) catalysts were prepared by a simple combustion method. Structure analysis by XRD, XPS, and TPR measurements revealed that the presence of three different CuO species: highly dispersed CuO, $Cu^{2+}$ in the $CeO_2$ lattice, and bulk CuO species. The distribution of Cu species in the $Cu_xCe_{1-x}O_y$ samples strongly depends on the Cu content: highly dispersed CuO and the $Cu^{2+}$ incorporate into the $CeO_2$ lattice coexist at low Cu/(Cu + Ce) ratio, while bulk CuO also formed besides the above two species at a higher Cu/(Cu + Ce) ratio. The activity of the catalysts for acetone combustion was dependent on the composition of the catalysts and the $Cu_{0.13}Ce_{0.87}O_y$ showed the highest catalytic activity. The pulse reaction of acetone in the absence of $O_2$ reveals a possibility of the involvement of a Mars–van Krevelen type mechanism in the acetone combustion over the $Cu_{0.13}Ce_{0.87}O_y$ catalyst. Both the GHSV and the acetone concentration have effect on the catalytic performance of the $Cu_{0.13}Ce_{0.87}O_y$ catalyst. Though exhibited a highly catalytic activity for acetone combustion, the $Cu_{0.13}Ce_{0.87}O_y$ catalyst had poor endurance in the catalytic combustion of acetone due to the formation of bulk CuO during the long-term test on stream. Further work is still under way for the improvement of the thermal stability of the $Cu_xCe_{1-x}O_y$ catalyst for acetone combustion.

## Acknowledgement

We would like to express our gratitude for financial support from National Natural Science Foundation of China (grant No. 20821092 and 20736004).

## References

[1] R. Atkinson, J. Arey, Atmospheric degradation of volatile organic compounds, Chem. Rev. 103 (2003) 4605–4638.
[2] H. Nakayama, A. Hayashi, T. Eguchi, N. Nakamura, M. Tsuhako, Adsorption of formaldehyde by polyamine-intercalated α-zirconium phosphate, Solid State Sci. 4 (2002) 1067–1070.
[3] K. Everaert, J. Baeyens, Catalytic combustion of volatile organic compounds, J. Hazard. Mater. B 109 (2004) 113–139.
[4] J.J. Spivey, Complete catalytic oxidation of volatile organics, Ind. Eng. Chem. Res. 26 (1987) 2165–2180.
[5] Y. Ma, M. Chen, C. Song, X. Zheng, Catalytic oxidation of toluene, acetone and ethyl acetate on a new Pt–Pd/stainless steel wire mesh catalyst, Acta Phys.: Chim. Sin. 24 (2008) 1132–1136.
[6] S. Minicò, S. Scirè, C. Crisafulli, S. Galvagno, Influence of catalyst pretreatments on volatile organic compounds oxidation over gold/iron oxide, Appl. Catal. B: Environ. 34 (2001) 277–285.
[7] V. Blasin-Aubé, J. Belkouch, L. Monceaux, General study of catalytic oxidation of various VOCs over $La_{0.8}Sr_{0.2}MnO_{3+x}$ perovskite catalyst-influence of mixture, Appl. Catal. B: Environ. 43 (2003) 175–186.
[8] R. Spinicci, M. Faticanti, P. Marini, S. De Rossi, P. Porta, Catalytic activity of $LaMnO_3$ and $LaCoO_3$ perovskites towards VOCs combustion, J. Mol. Catal. A: Chem. 197 (2003) 147–155.
[9] M. Paulis, L.M. Gandía, A. Gil, J. Sambeth, J.A. Odriozola, M. Montes, Influence of the surface adsorption–desorption processes on the ignition curves of volatile organic compounds (VOCs) complete oxidation over supported catalysts, Appl. Catal. B: Environ. 26 (2000) 37–46.
[10] L.M. Gandía, M.A. Vicente, A. Gil, Complete oxidation of acetone over manganese oxide catalysts supported on alumina- and zirconia-pillared clays, Appl. Catal. B: Environ. 38 (2002) 295–307.
[11] A. Trovarelli, Catalytic properties of ceria and $CeO_2$-containing materials, Catal. Rev. Sci. Eng. 38 (1996) 439–520.
[12] R.J. Gorte, S. Zhao, Studies of the water–gas-shift reaction with ceria-supported precious metals, Catal. Today 104 (2005) 18–24.
[13] W. Shan, M. Luo, P. Ying, W. Shen, C. Li, Reduction property and catalytic activity of $Ce_{1-x}Ni_xO_2$ mixed oxide catalysts for $CH_4$ oxidation, Appl. Catal. A: Gen. 246 (2003) 1–9.
[14] N. Imanaka, T. Masui, K. Koyabu, K. Minami, T. Egawa, Significant low-temperature redox activity of $Ce_{0.64}Zr_{0.16}Bi_{0.20}O_{1.90}$ supported on $\gamma$-$Al_2O_3$, Adv. Mater. 19 (2007) 1608–1611.
[15] D. Delimaris, T. Ioannides, VOC oxidation over $MnO_x$–$CeO_2$ catalysts prepared by a combustion method, Appl. Catal. B: Environ. 84 (2008) 303–312.
[16] G. Picasso, M. Gutiérrez, M.P. Pina, J. Herguido, Preparation and characterization of Ce–Zr and Ce–Mn based oxides for n-hexane combustion: application to catalytic membrane reactors, Chem. Eng. J. 126 (2007) 119–130.
[17] X. Tang, J. Chen, Y. Li, Y. Li, Y. Xu, W. Shen, Complete oxidation of formaldehyde over Ag/$MnO_x$–$CeO_2$ catalysts, Chem. Eng. J. 118 (2006) 119–125.
[18] A. Martínez-Arias, D. Gamarra, M. Fernández-García, X.Q. Wang, J.C. Hanson, J.A. Rodriguez, Comparative study on redox properties of nanosized $CeO_2$ and $CuO/CeO_2$ under $CO/O_2$, J. Catal. 240 (2006) 1–7.
[19] G. Avgouropoulos, J. Papavasiliou, T. Tabakova, V. Idakiev, T. Ioannides, A comparative study of ceria-supported gold and copper oxide catalysts for preferential CO oxidation reaction, Chem. Eng. J. 124 (2006) 41–45.
[20] D. Delimaris, T. Ioannides, VOC oxidation over CuO–$CeO_2$ catalysts prepared by a combustion method, Appl. Catal. B: Environ. 89 (2009) 295–302.
[21] X. Tang, Y. Xu, W. Shen, Promoting effect of copper on the catalytic activity of $MnO_x$–$CeO_2$ mixed oxide for complete oxidation of benzene, Chem. Eng. J. 144 (2008) 175–180.
[22] J. Kaspar, P. Fornasiero, G. Balducci, R.D. Monte, N. Hickey, V. Sergo, Effect of $ZrO_2$ content on textural and structural properties of $CeO_2$–$ZrO_2$ solid solutions made by citrate complexation route, Inorg. Chim. Acta 349 (2003) 217–226.
[23] T. Mokkelbost, I. Kaus, T. Grande, M.-A. Einarsrud, Combustion synthesis and characterization of nanocrystalline $CeO_2$-based powders, Chem. Mater. 16 (2004) 5489–5494.
[24] A. Tschöpe, M.L. Trudeau, J.Y. Ying, Redox properties of nanocrystalline Cu-doped cerium oxide studied by isothermal gravimetric analysis and X-ray photoelectron spectroscopy, J. Phys. Chem. B 103 (1999) 8858–8863.
[25] A. Martínez-Arias, M. Fernández-García, O. Gálvez, J.M. Coronado, J.A. Anderson, J.C. Conesa, J. Soria, G. Munuera, Comparative study on redox properties and catalytic behavior for CO oxidation of CuO/$CeO_2$ and CuO/$ZrCeO_4$ catalysts, J. Catal. 195 (2000) 207–216.
[26] T. Tabakova, V. Idakiev, J. Papavasiliou, G. Avgouropoulos, T. Ioannides, Effect of additives on the WGS activity of combustion synthesized CuO/$CeO_2$ catalysts, Catal. Commun. 8 (2007) 101–106.
[27] B.M. Reddy, A. Khan, Y. Yamada, T. Kobayashi, S. Loridant, J.-C. Volta, Raman and X-ray photoelectron spectroscopy study of $CeO_2$–$ZrO_2$ and $V_2O_5$/$CeO_2$–$ZrO_2$ catalysts, Langmuir 19 (2003) 3025–3030.
[28] C.D. Wagner, W.M. Riggs, L.E. Davis, J.F. Moulder, G.E. Muilenberg, Handbook of X-Ray Photoelectron Spectroscopy, Perkin-Elmer Corp., Palo Alto, CA, 1978.
[29] C.-H. Wang, S.-S. Lin, C.-L. Chen, H.-S. Weng, Performance of the supported copper oxide catalysts for the catalytic incineration of aromatic hydrocarbons, Chemosphere 64 (2006) 503–509.
[30] W. Liu, M. Flytzani-Stephanopoulos, Transition metal-promoted oxidation catalysis by fluorite oxides: a study of CO oxidation over Cu–$CeO_2$, Chem. Eng. J. 64 (1996) 283–294.
[31] M.-F. Luo, Y.-P. Song, X.-Y. Wang, G.-Q. Xie, Z.-Y. Pu, P. Fang, Y.-L. Xie, Preparation and characterization of nanostructured $Ce_{0.9}Cu_{0.1}O_{2-\delta}$ solid solution with high surface area and its application for low temperature CO oxidation, Catal. Commun. 8 (2007) 834–838.
[32] S.-P. Wang, X.-C. Zheng, X.-Y. Wang, S.-R. Wang, S.-M. Zhang, L.-H. Yu, W.-P. Huang, S.-H. Wu, Comparison of CuO/$Ce_{0.8}Zr_{0.2}O_2$ and CuO/$CeO_2$ catalysts for low-temperature CO oxidation, Catal. Lett. 105 (2005) 163–168.
[33] G. Avgouropoulos, T. Ioannides, Effect of synthesis parameters on catalytic properties of CuO–$CeO_2$, Appl. Catal. B: Environ. 67 (2006) 1–11.
[34] L. Lisi, G. Bagnasco, P. Ciambelli, S.D. Rossi, P. Porta, G. Russo, M. Turco, Perovskite-type oxides. II. Redox properties of $LaMn_{1-x}Cu_xO_3$ and

$LaCo_{1-x}Cu_xO_3$ and methane catalytic combustion, J. Solid State Chem. 146 (1999) 176–183.
[35] N. Burgos, M. Paulis, M.M. Antxustegi, M. Montes, Deep oxidation of VOC mixtures with platinum supported on $Al_2O_3$/Al monoliths, Appl. Catal. B: Environ. 38 (2002) 251–258.
[36] R.J.H. Voorhoeve, J.P. Remeika, D.W. Johnson, Rare-earth manganites: catalysts with low ammonia yield in the reduction of nitrogen oxides, Science 180 (1973) 62–64.
[37] E. Finocchio, R.J. Willey, G. Busca, V. Lorenzelli, FTIR studies on the selective oxidation and combustion of light hydrocarbons at metal oxide surfaces, J. Chem. Soc., Faraday Trans. 93 (1997) 175–180.
[38] M. Baldi, F. Milella, G. Ramis, V. Sanchez Escribano, G. Busca, An FT-IR and flow reactor study of the selective catalytic oxy-dehydrogenation of C3 alcohols on $Mn_3O_4$, Appl. Catal. A: Gen. 166 (1998) 75–88.
[39] L.M. Gandía, A. Gil, S.A. Korili, Effects of various alkali–acid additives on the activity of a manganese oxide in the catalytic combustion of ketones, Appl. Catal. B: Environ. 33 (2001) 1–8.
[40] A. Martínez-Arias, M. Fernández-García, J. Soria, J.C. Conesa, Spectroscopic study of a $Cu/CeO_2$ catalyst subjected to redox treatments in carbon monoxide and oxygen, J. Catal. 182 (1999) 367–377.